ADVANCING EARTH AND SPACE SCIENCE

Geochemistry, Geophysics, Geosystems

RESEARCH ARTICLE
10.1029/2019GC008883

Key Points:
- We provide an open-access VPSC library of elastic tensors for *D″* seismic anisotropy observations
- We compare multiple regional *D″*-associated shear wave splitting data sets and core-mantle boundary flow models to the library
- This study shows bridgmanite provides a poor fit to seismic data, while ferropericlase and postperovskite have the best fit

Supporting Information:
- Supporting Information S1
- Table S1–S7
- Table S8–S17

Correspondence to:
N. Creasy,
neala.creasy@yale.edu

Citation:
Creasy, N., Miyagi, L., & Long, M. D. (2020). A library of elastic tensors for lowermost mantle seismic anisotropy studies and comparison with seismic observations. *Geochemistry, Geophysics, Geosystems*, *21*, e2019GC008883. https://doi.org/10.1029/2019GC008883

Received 23 DEC 2019
Accepted 24 MAR 2020
Accepted article online 26 MAR 2020

A Library of Elastic Tensors for Lowermost Mantle Seismic Anisotropy Studies and Comparison With Seismic Observations

Neala Creasy[1,2], Lowell Miyagi[3], and Maureen D. Long[1]

[1]Department of Geology and Geophysics, Yale University, New Haven, CT, USA, [2]Department of Geophysics, Colorado School of Mines, Golden, CO, USA, [3]Department of Geology and Geophysics, University of Utah, Salt Lake City, UT, USA

Abstract The exact mechanism for lowermost mantle seismic anisotropy remains unknown; however, work on the elasticity and deformation of lower mantle materials has constrained a few possible options. The most probable minerals producing anisotropy are bridgmanite, postperovskite, and ferropericlase. While there is an extensive literature on the elasticity and deformation of lower mantle minerals, we create a comprehensive uniform database of *D″* anisotropy scenarios. In order to characterize a range of the possible fabrics for *D″* anisotropy, we carry out VPSC (visco-plastic self-consistent modeling) to predict textures for each proposed mineral and dominant slip system. We numerically deform each mineral under different geometrical scenarios: simple shear, pure shear, and extension. By using published single crystal elasticity values, we produce a library of 336 candidate elastic tensors. We used the elastic tensor library to revisit previously published *D″*-associated seismic anisotropy studies for crossing raypaths (Siberia, North America, the Afar region of Africa, and Australia). While we cannot identify a single, unique mechanism that explains all of these data sets, we find that postperovskite (dominant slip on [100](010) or [100](001)) and periclase (dominant slip on {100}<011>) provide the best fit to the observations and suggest reasonable shear directions for each region of interest. Bridgmanite generally provides a poor fit to the observations; however, we cannot completely rule out any particular model. As the number of anisotropy observations for *D″* increases, this elastic tensor library will be helpful for observational seismologists in identifying possible mechanisms of anisotropy and shear directions at in the lowermost mantle.

Plain-Language Summary At 2,800 km below the Earth's surface, minerals are being deformed under the high pressures, temperatures, and stresses of the deep mantle. A seismic phenomenon (seismic anisotropy) has been observed within this region, likely due to the deformation of some unknown mineral. There have been three proposed minerals based on experimental and theoretical work. As a result, we create a library of proposed mechanisms of this anisotropy by numerically calculating a series of plausible deformed rocks with a code called VPSC (viscoplastic self-consistent modeling). We have established an open-source library of elastic tensors (plausible deformed rocks) for all of the proposed minerals. We compare this library to data that have been previously observed near the core-mantle boundary (Siberia, North America, the Afar region of Africa, and Australia). We find that some of the tensors cannot consistently fit all of the available data sets (such as bridgmanite—the most abundant mineral in the lower mantle). However, two of the minerals can fit all of the data quite well (postperovskite and ferropericlase). Postperovskite is a result of bridgmanite changing its structure due to the high pressures and temperatures, approximately 200 km above the core-mantle boundary, and the lower mantle consists of ~20% ferropericlase.

1. Introduction

The *D″* region at the base of the mantle hosts the thermochemical boundary between the mantle and core, large gradients in seismic velocities, and continent-sized heterogeneities (i.e., Large Low Shear Velocity Provinces or LLSVPs). The still-enigmatic nature of the lowermost mantle has inspired much study on the structure, dynamics, and material properties of the *D″* region. One remarkable observation of *D″* is the presence of seismic anisotropy—a feature that has been observed since the 1990s (Lay & Young, 1991; Maupin, 1994; Vinnik et al., 1995). Since then, there have been major strides in collecting more observations and understanding plausible mechanisms of anisotropy. However, an agreed-upon framework does not yet exist to directly relate D'' seismic anisotropy observations to deformation (i.e., mantle flow) (Nowacki et al., 2011). In contrast, such a framework is widely used for the upper mantle (e.g., Long & Becker, 2010), invoking lattice preferred orientation (LPO) of olivine aggregates. A key first step to understand flow at the base of the mantle is to understand the mechanism of D'' anisotropy, that is, which materials are responsible for anisotropy and how the anisotropy relates to deformation.

Even after nearly 30 years of observing seismic anisotropy in the lowermost mantle, we have yet to uniquely constrain one responsible mechanism for D'' anisotropy of the many proposed. Recent modeling work has demonstrated that an unrealistic amount of body wave data is required to uniquely constrain a particular mechanism or its orientation (Creasy et al., 2019) in a specific region. In order to constrain anisotropy tightly, reasonable backazimuthal coverage is generally required (Chevrot, 2000; Savage, 1999). This condition is simpler to achieve for the upper mantle as compared to D'', as reasonable backazimuthal coverage can be attained using a single station. For D'', a promising observational strategy is to identify earthquake-receiver pairs that have intersecting raypaths within D'', utilizing many stations and events. An additional challenge is that seismic stations must also be located above upper mantle with simple anisotropic structure in order to remove the upper mantle effects on raypaths that propagate through the D'' layer. (We typically assume that measurements only reflect D'' and upper mantle anisotropy; contributions from the crust and from the bulk of the lower mantle are typically neglected.)

The lower mantle is predicted to consist of 76% bridgmanite (Bm) $MgSiO_3$, 17% ferropericlase (Fp) (Mg,Fe)O, and 7% calcium perovskite $CaSiO_3$ (Lee et al., 2004). In the D'' layer, bridgmanite may undergo an isochemical phase change to postperovskite (Ppv). Bm, Fp, and Ppv are considered to be plausible candidates for the mechanism of D'' anisotropy. Calcium perovskite is volumetrically a minor phase in the lower mantle and is not considered as a plausible candidate. Proposed models for D'' anisotropy are typically based on ab initio calculations of elasticity of candidate minerals in combination with deformation experiments, done at low-pressure/high-temperature or high-pressure/low-temperature conditions (as summarized by Nowacki et al., 2011). For example, postperovskite is not stable at ambient conditions and cannot be deformed in a multianvil press at lab conditions; it can only be deformed in smaller volumes within diamond anvil cells (e.g., Murakami et al., 2004). Experiments on polycrystalline materials, such as ferropericlase and analog materials of postperovskite—similar in structure to postperovskite but of a different composition (e.g., $CaIrO_3$: Yamazaki et al., 2006)—are extrapolated to D'' conditions. There is a wide range of models for D'' anisotropy that have been proposed, invoking various dominant slip systems for any given mineral (based on different types of experiments, e.g., multianvil vs. diamond anvil cell), ab initio single-crystal calculations, considerations of polyphase aggregates (e.g., postperovskite mixed with ferropericlase), deformation geometry, amount of strain, and possible presence of impurities, such as iron and aluminum (Caracas, 2010; Stackhouse et al., 2005). Observational studies of D'' anisotropy have been inconsistent as to which elasticity models are tested against observational constraints because of the availability of so many proposed models, making it difficult to compare inferences from different seismic observational studies. For example, some studies only consider single crystal elastic tensors (e.g., Ford et al., 2015), while others rely on models that represent polycrystalline fabrics derived using tools such as visco-plastic self-consistent (VPSC) modeling (Lebensohn & Tomé, 1994) or use models based on constraints from multianvil cell experiments (e.g., Wookey & Kendall, 2008).

VPSC is a widely used and powerful tool to model deformation and anisotropy development. For example, one can model texture development along streamlines in a particular flow regime, such as a slab or plume configuration (e.g., Cottaar et al., 2014; Walker et al., 2011). Such studies are very useful in predicting elastic tensors for a particular flow model within a particular regional framework; however, it is often difficult to extrapolate these models to other regions in D'' and apply them widely to shear wave splitting data sets. These modeling studies also make assumptions on the mechanism of anisotropy, dominant slip system, and among others, and different choices in building a flow model may drastically change the resulting predicted anisotropy. There is, therefore, a need for a comprehensive uniform database of possible elasticity scenarios (beyond single crystal estimates) for the lowermost mantle for simple endmember deformation scenarios.

In this study, we develop a library of models of seismic anisotropy in D'' in the form of elastic tensors (a total of 336 elastic tensors) that were calculated under a wide range of plausible assumptions for deformation

10.1029/2019GC008883

geometry, properties of single crystal elastic tensors, mineralogy, slip systems, and strain. We then compare a subset of this database to a set of previously published observations of D''-associated shear wave splitting. These comparisons against a range of splitting observations that include observations over multiple azimuths have identified three plausible mechanisms that suggest reasonable shear directions for each region and are consistent across study regions: ferropericlase with dominant slip on {100}<011>, postperovskite with dominant slip on (010)[100], and postperovskite with dominant slip on (001)[100]. With additional future observations of D'' anisotropy, it is likely that we can constrain the responsible mechanism even further, using the elastic tensor library presented here. The long-term goal of this work is to establish a framework that relates seismic anisotropy observations and flow at the base of the mantle.

2. Methods

2.1. Forming an Elastic Tensor Library: Viscoplastic Self-Consistent Models

To form our elastic tensor library, we use the Los Alamos VPSC Version 6 (Lebensohn & Tomé, 1994) to simulate the formation of texture (crystal preferred orientation) for a range of proposed minerals and slip systems under a few specific deformation scenarios. VPSC has been widely used to simulate texture development associated with experimental deformation and industrial processing in a wide range of metals, ceramics, and minerals (e.g., Tome & Canova, 2000; Wenk, 2000) and has been applied to model complex deformation geometries associated with geologic phenomena (e.g., Romanowicz & Wenk, 2017). VPSC treats each grain as an inclusion in a homogeneous but anisotropic matrix, where the properties of the matrix are an average of the individual grains. At each incremental deformation step, the inclusions interact and are updated in the loop until the average stress/strain of all the inclusions is consistent with the macroscopic stress/strain. Texture development depends on the deformation geometry, relative activities of various deformation modes (slip and twinning), and the total strain. As deformation proceeds, crystals deform and rotate to generate a preferred orientation. Slip system and twin mode activities are determined by the orientation of slip planes and slip directions, their symmetric variants, and the corresponding rate-sensitive critical resolved shear stresses (CRSSs).

For these simulations we use 2,000 grains with a tangent linearization scheme for the inclusion matrix interaction. The tangent method allows for heterogeneous grain to grain deformation and generally lies between the Sachs (stress compatibility) and Taylor (strain compatibility) bounds (e.g., Lebensohn et al., 2011). We test three endmember deformation geometries of simple shear, pure shear, and axial extension. More specifically, when referring to pure shear, the deformation is constrained to plane strain, with stretching in both the positive and negative x direction and shortening along the y axis. Strain in the z direction is fixed to zero. Also, axial extension is equivalent to constriction, where compression occurs along two axes (y and z) and stretching along one axis (x). This results in hexagonal symmetry about the x axis (see Figure 1). As a large portion of deformation in the lower mantle is likely accommodated by diffusion processes, we assume that only a small proportion of the total strain is accommodated by dislocations. We conduct these simulations with 50% and 100% strain in 2% strain increments. VPSC uses rate-sensitive plasticity; for silicate phases bridgmanite and postperovskite, we use a stress exponent of $n = 3$, and for ferropericlase, we use $n = 5$. For silicates and oxides, stress exponents are typically in the range of $n = 3–5$ (e.g., Karato, 2008). Here we choose $n = 3$ for bridgmanite and postperovskite following Wenk et al. (2006, 2011). Ferropericlase appears to have a slightly higher stress exponent (e.g., Stretton et al., 2001); therefore, we chose a stress exponent of $n = 5$, as was done in Immoor et al. (2018). As noted in Immoor et al. (2018), increasing the stress exponent by 1 or 2 does not have a significant effect on texture evolution.

Once texture development is simulated for the various deformation geometries and CRSS weights, the orientation sets are exported to Beartex (Wenk et al., 1998), where each set of orientations is used to calculate an orientation distribution function (ODF). The ODF is smoothed with a 7.5° Gauss filter. Single crystal elastic constants are then averaged over the ODF to calculate a polycrystalline elastic tensor using a geometric mean (Matthies & Humbert, 1993). Multiphase polycrystalline tensors are similarly calculated with a geometric mean assuming a 75:25 ratio of bridgmanite/postperovskite and ferropericlase. Figure 1 illustrates three end-member deformation cases, how they affect the rotation of grains within the polycrystalline material, and the resulting prediction of Vp and Vs anisotropy, using postperovskite as an example. The Vp and Vs anisotropies are calculated using the MSAT toolkit (Walker & Wookey, 2012).

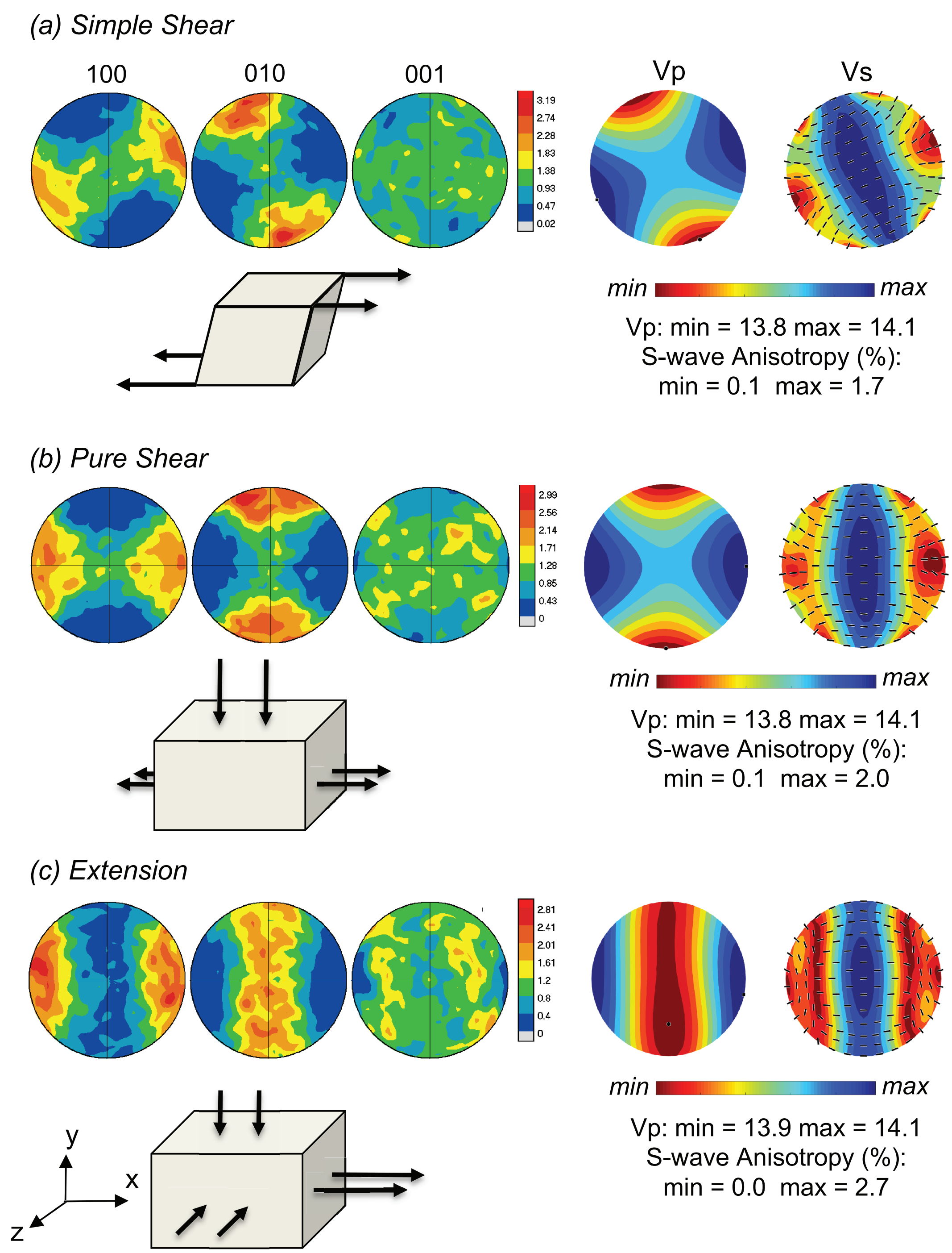

Figure 1. Example VPSC results for postperovskite deformed with the dominant slip system (010)[100] at 100% strain for three different deformation scenarios: (a) simple shear, (b) pure shear, and (c) extension. (Left three images) pole figures of the orientations of [100], [010], and [001] axes. Boxes and arrows show the deformation geometry for each scenario, in which inward arrows show compression and outward arrows show extension. Colors represent density of grains as a result of texture development in multiples of uniform distribution (m.u.d.). (Right three images) Stereoplots of seismic anisotropy for Vp and Vs for the textures shown in the left panels, where colors represent strength of anisotropy (%). For Vs, black bars represent fast splitting directions prediction in ray reference frame. The shear direction is in the *x* direction (to the right) and the shear normal is in the *y* direction (upward).

Table 1
Summary of Candidate Minerals and Slip Systems Examined in This Work

Mineral	Starting single crystal	Reference for single crystal	Slip system(s)	Reference for slip system(s)
Bridgmanite (Br)	*125 GPa, 2,500 K	A	High pressure and high temperature: (100)[010] + (100)[011]	1,2
	126 GPa, 2,800 K	B		
	136 GPa, 4,000 K		Low pressure and low temperature: (001)	3
Ferropericlase (Fp)	*135 GPa, 3,000 K	C	High temperature: {100}<011>	4,5,6,7
			Low temperature: {110} < 1–10>	8,9
Postperovskite (Ppv)	*125 GPa, 2,500 K	A	Ppv 1: (010)[100]	10,11,12
	140 GPa, 4,000 K		Ppv 2: (001)[100]	13,14
	135 GPa, 4,000 K	D	Ppv 3: {011}< 0–11> + (010)<100>	15
	136 GPa, 3,000 K			

Note. Table shows minerals, starting single crystals (given in pressure and temperature conditions and citation), and dominant slip systems for scenarios included in the elastic tensor library. For bridgmanite and ferropericlase, we examine both slip systems that are preferred for midmantle pressures (low pressure and temperature) and those preferred for the lowermost mantle (high pressure and temperature). References: (1) Tsujino et al. (2016); (2) Couper et al. (2018); (3) Miyagi & Wenk, 2016; (4) Immoor et al. (2018); (5) Amodeo et al. (2012); (6) Cordier et al. (2012); (7) Girard et al. (2012); (8) Merkel et al. (2002); (9) Lin et al. (2019); (10) Miyagi et al. (2008); (11) Yamazaki et al. (2006); (12) Kubo et al. (2008); (13) Hirose et al. (2010); (14) Miyagi et al. (2010); (15) Lin and Miyagi (2017); (A) Wentzcovitch et al. (2006); (B) Wookey, Stackhouse, et al. (2005); (C) Karki et al. (1999); (D) Stackhouse et al. (2005).
*Tensors used for the forward modeling component with shear wave splitting data sets.

For the weighting of CRSS values, we test a range of dominant slip system values as proposed in the literature. Table 1 summarizes all minerals and dominant slip systems included in the elastic tensor library. In an attempt to create a consistent and comprehensive library, we invoked recent and plausible results on the most probable dominant slip systems for each proposed mineral. For ferropericlase elasticity, we test dominant {100}<011> slip using CRSS values from Immoor et al. (2018), which is preferred for higher temperatures in the lower mantle. We also include lower temperature dominant {110}<1–10> slip using the CRSS values of Lin et al. (2019). These slip systems are in agreement with various experimental and theoretical results where {110} slip dominates at low temperature and pressure, and slip on {100} becomes favorable under lowermost mantle conditions (high-pressure and high-temperature conditions). In this study, we only compare the dominant slip systems preferred at high pressure and temperature with the seismic observations but include the lower-temperature-preferred slip systems in the library. For our calculations of effective anisotropy we use pure MgO single crystal based on Karki et al. (1999) at 135 GPa and 3,000 K. The lower-pressure elastic tensors in Table 1 should be a useful tool for seismic anisotropy studies in the top of the lower mantle, where seismic anisotropy has been observed beneath subducting slabs (e.g., Faccenda, 2014; Lynner & Long, 2014a).

For bridgmanite, we test dominant (100)<010> + (100)<011> slip based on the high-temperature diamond anvil cell deformation data of Couper et al. (2018). Notably, these CRSS values also provide a good fit to the data of Tsujino et al. (2016) when used in simple shear simulations (Couper et al., 2018). We also include in the library a preferred dominant (001) slip using the CRSS values from Miyagi and Wenk (2016) “Model l.” Miyagi and Wenk (2016) showed that bridgmanite's dominant slip plane changes with pressure, where (001) dominates at pressures less than 55 GPa and (100) dominates at higher pressures. We only compare the higher-pressure slip system to the seismic observations but include the lower-pressure slip system in the library, as the lower-pressure preferred slip system of (001) may be useful for seismic anisotropy studies at the top of the lower mantle. We use a starting single-crystal anisotropic elastic tensor (Wentzcovitch et al., 2006) at 125 GPa and 2,500 K for the seismic comparisons. However, other proposed single-crystal elastic tensors of Wookey, Stackhouse, et al. (2005) are included in the library.

Postperovskite has many proposed slip systems. Based on the most recent work, we model three different plausible slip systems that we will refer to as Ppv 1, Ppv 2, and Ppv 3 throughout this study. Ppv 1 invokes dominant slip on (010)[100]; this dominant slip system is observed in a number of experimental studies on the postperovskite analog $CaIrO_3$ (Miyagi et al., 2008; Yamazaki et al., 2006). Ppv 2 represents the (001)[100] dominant slip system, as proposed based on laser-heated diamond anvil cell experiments on $MgSiO_3$ and postperovskite analogs $MgGeO_3$ and $MnGeO_3$ (Hirose et al., 2010; Miyagi et al., 2010, 2011; Okada et al., 2010; Wu et al., 2017). Ppv 3 simulates postperovskite deformed with a combination of (010), (001), and {011} slip from Lin and Miyagi (2017). These were obtained by using the Elasto-Visco Plastic

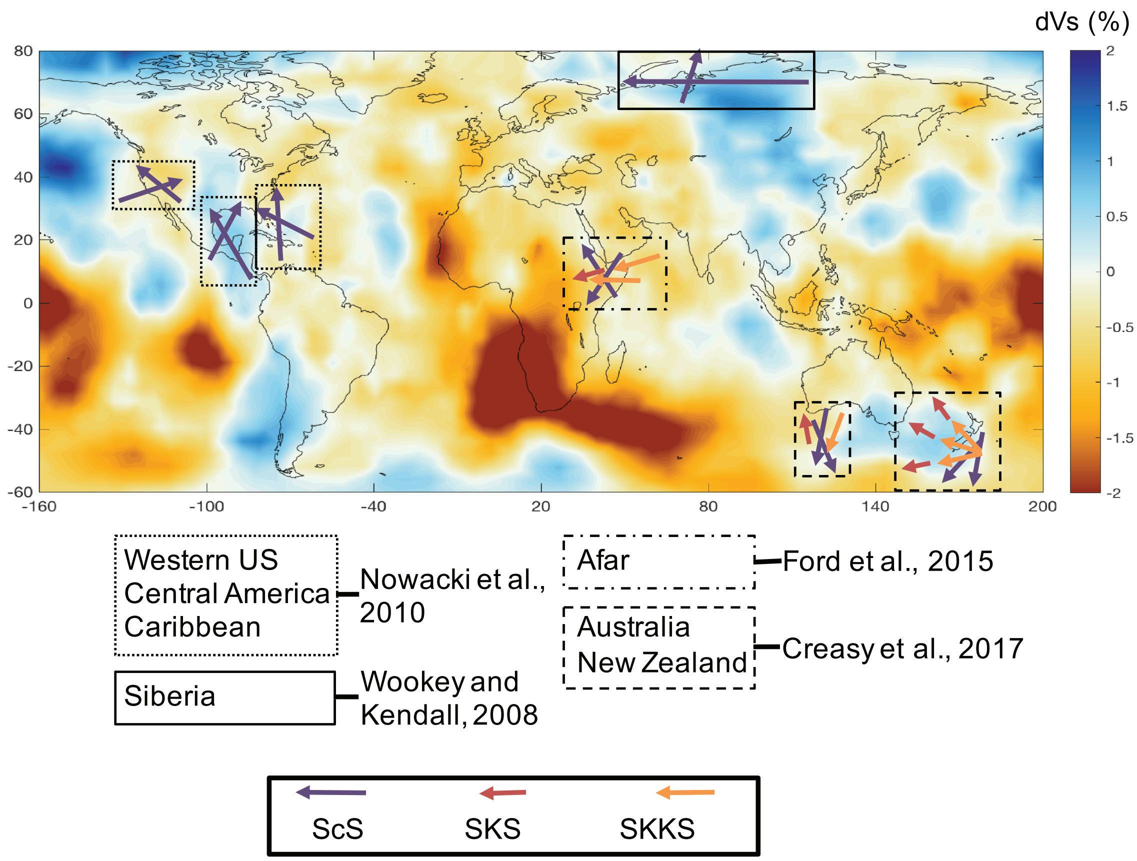

Figure 2. Map of all shear wave splitting data sets used in this study, identified with boxes. Data sets that only include ScS measurements (purple arrows, representing the portion of the raypath that travels through the D'' layer) sample beneath North America (Nowacki et al., 2010) and beneath Siberia (Wookey & Kendall, 2008). Ford et al. (2015) observed shear wave splitting for ScS, SKS (red arrows), and SKKS (orange arrows) beneath the Afar plume. Creasy et al. (2017) observed shear wave splitting for ScS, SKS, and SKKS beneath the southwestern edge of Australia and beneath New Zealand. For SKS and SKKS phases, we exaggerate the length of the D'' portion of the raypath by four times for visibility.

Self-Consistent (Wang et al., 2010; Lin et al., 2017) approach to simulate lattice strain and texture evolution of the silicate postperovskite data of Miyagi et al. (2010). Note that we do not test slip on (100) or {110}<1–10> slip, as proposed to explain textures observed in Merkel et al. (2007, 2006); these textures were later shown to be generated during the enstatite to postperovskite transformation rather than through deformation (Miyagi et al., 2011; Okada et al., 2010). We use the starting single-crystal elasticity of Wentzcovitch et al. (2006) at 125 GPa and 2,500 K for all three simulated slip systems when comparing to the seismic observations. We also included other starting single crystals within the library, specifically the estimates from Stackhouse et al. (2005).

2.2. Comparison With Seismic Observations

In order to compare the predictions from our library of elastic tensors to recent observations, we considered a range of D''-associated shear wave splitting data sets, for which any upper mantle contribution to splitting has been removed. Creasy et al. (2019) showed that at least two crossing raypaths are needed to uniquely constrain a candidate elastic tensor and its possible orientation. We therefore considered every published study that has measured shear wave splitting due to D'' anisotropy with at least two crossing raypaths. This yielded a total of seven unique regional data sets derived from four different studies (Figure 2).

There are many seismic phases that propagate through D''; however, SKS and SKKS (e.g., Lynner & Long, 2014b), PcS (He & Long, 2011), S_{diff} (Cottaar & Romanowicz, 2013), and ScS (Wookey, Kendall, et al., 2005) are the only phases that have been successfully measured for D''-associated splitting with the removal of the upper mantle component. We will only focus on SKS, SKKS, and ScS because these are the phases that have been analyzed with crossing raypaths. SKS and SKKS are phases that originate as an *S* wave at the source, propagate through the liquid outer core as a *P* wave, and then exit the outer core as an *S* wave. SKKS has an internal reflection within the outer core, resulting in a shallower inclination angle than SKS as SKKS exits the core. ScS reflects off the core-mantle boundary (CMB) and propagates along the CMB at a shallow angle from the horizontal at the distance ranges considered in D'' anisotropy studies (60–80°). SKS and SKKS are commonly used to constrain the upper mantle anisotropy beneath a single station, but some studies have had success in measuring the D'' contribution to the splitting of SK(K)S phases. Wookey, Kendall, et al. (2005) and Lynner and Long (2014b) contain thorough discussion about the methods used to measure D'' shear wave splitting, including how the upper mantle contribution to splitting is removed.

Two of the studies that we consider here observed ScS shear wave splitting for intersecting paths beneath North America, Central America, and the Caribbean (Nowacki et al., 2010) and beneath Siberia (Wookey & Kendall, 2008). The other two studies combined SKS, SKKS, and ScS shear wave splitting to sample the lowermost mantle beneath the Afar region of Africa (Ford et al., 2015), as well as beneath southwestern Australia and New Zealand (Creasy et al., 2017). Figure 2 summarizes all of the data sets used in this study.

To test whether a given elastic tensor is consistent with a given set of D'' anisotropy observations, we carried out forward modeling based on the framework used by Ford et al. (2015) and Creasy et al. (2017). First, we assume that the anisotropic structure is laterally homogenous within each region and thus that each of the individual raypaths is sampling the same anisotropy. Our modeling scheme invokes ray theoretical predictions of shear wave splitting; however, finite frequency effects should be considered in future work (e.g., Nowacki & Wookey, 2016). We calculate an average straight line approximation through D'' for each group of raypaths. We estimate D'' thickness, which we assume is the thickness of the anisotropic layer, from previous studies of the D'' discontinuity in each of these regions: Western United States, 250 km (Young & Lay, 1990); Central America, 270 km (Lay & Helmberger, 1983); Caribbean, 270 km (Lay & Helmberger, 1983); Siberia, 300 km (Weber & Davis, 1990); Afar, 280 km (Indian Ocean: Young & Lay, 1987); Australia, 250 km (Kendall & Shearer, 1994); and New Zealand, 350 km (Usui et al., 2005). For SKS and SKKS, we calculated propagation angles (from the horizontal) of each group of raypaths using TauP (Crotwell et al., 1999) with the *ak135* velocity model (Kennett et al., 1995). For ScS, we assumed horizontal propagation through D'' (a common assumption used in each of the studies utilized here), although propagation angles can vary from the horizontal up to 15°. We transformed the splitting measurements into a ray-centered coordinate system or used the reported ray-centered measurements from each study, following Nowacki et al. (2010).

To test for consistency between splitting observations and predictions from our modeled elastic tensors, we rotated each candidate elastic tensor from the library in 5° increments around each of the three rotation axes. For each candidate orientation, we calculated the predicted splitting parameters for each group of raypaths (as identified by arrows in Figure 2) using representative azimuth and inclination values, by solving the Christoffel equation using the MSAT toolkit (Walker & Wookey, 2012). We calculated a misfit value based on a residual sum of squares approach between each observed splitting parameter and the corresponding predicted splitting parameter at every orientation for each candidate tensor, following Ford et al. (2015). For the fast directions, the misfit calculation is straightforward. We consider a prediction to successfully match a split measurement if both misfit criteria are met: (1) The predicted (scaled) delay time is greater than the 0.5 s cutoff and (2) the predicted fast or slow direction is within 20° of the observed fast-axis direction. The entire data set must fit within these constraints to be an acceptable model and orientation. We use a consistent 20° error cutoff for every group of observations no matter the reported errors in fast-axis directions. The observed fast direction cannot exceed the predicted fast direction by more than this amount, which is a typical maximum error often reported in splitting studies.

Delay times, however, are a function of strain, anisotropic layer thickness, orientation of the elastic tensor, and path length through the anisotropic material. Due to the number of unknown parameters, we considered two different approaches to estimating delay times, considering both predicted absolute delay times and predicted relative delay times. For the first method, we required that all split observations must result in predicted delay times greater than 0.5 s, whereas all observed null measurements must result in predicted delay times less than 0.5 s. The selection of 0.5 s represents a typical cutoff for a null measurement (put another way, our observational strategy cannot constrain splitting with a delay time of less than 0.5 s).

10.1029/2019GC008883

With relative delay times, we use ratios of the predicted delay times compared to the maximum predicted delay time from each corresponding elastic tensor. These ratios are then compared to the observed data by relating all observed delay times to the maximum observed delay time.

There are many null measurements in several of these data sets; particularly Afar, New Zealand, and Australia. The treatment of null (i.e., not split) measurements in the forward modeling is an important consideration, as a null observation can be either due to weak/nonexistent anisotropy or to the alignment of the initial polarization of the incoming wavelet with the fast or slow directions of anisotropic symmetry. The initial polarizations from the waveform for all null ScS waves were reported in these studies. For SK(K)S phases, the polarization is constrained to be equivalent to the back azimuth by the *P*-to-*S* conversion at the CMB and is the same for the entire group of raypaths. Our modeling approach takes into account both possible scenarios for the null observations. For paths along which we observe only null measurements, we take into account the possibility of weak anisotropy by implementing a cutoff of 0.5 s delay time, in which a model is discarded if it predicts more than 0.5 s of splitting for a path that exhibits no splitting in the data. We consider a prediction to successfully match a null observation if either (1) the predicted (scaled) delay time is less than the 0.5 s cutoff or (2) the predicted fast or slow direction is within 10° of the initial polarization (ScS) or the back azimuth (SK(K)S) direction.

For each candidate elastic tensor in the library and regional data set, we eliminate a single orientation of that elastic tensor if any of the raypaths within each data set breaks one of our criteria listed above as inconsistent with the observations. If all tested orientations for one elastic tensor and one data set fail to pass our misfit criteria, then we can rule out that model completely.

2.3. Comparing Shear Directions With Flow Model Predictions

In order to evaluate the geodynamic implications of the best fit directions for each regional data set and elastic tensor, we interrogated two different previously published flow models to give a sense for plausible flow directions in each region (Figure 3). As a simplified first step, we use velocity vectors as a comparison to plausible shear directions inferred from our modeling; this assumption implicitly accepts that a local gradient in velocity magnitude results in the accumulation of finite strain. (Of course, a consideration of the full finite strain field is needed for a more complete comparison; this will be carried out in future work.) The first flow model is based on a mantle convection simulation using plate reconstructions from the past 230 Ma, including dynamic topography data, locations of subducting slabs, locations of LLSVPs, and global tomography models (Flament, 2019: Case 3). The other flow model (Forte et al., 2015) is based on a joint inversion of GyPSuM tomography (Simmons et al., 2010), global gravity field, dynamic surface topography, tectonic plate motions, excess ellipticity of the CMB, and a specified viscosity profile (Profile V1 in Mitrovica & Forte, 2004). The flow models are shown in Figure 3, with the pink boxes showing the regional locations of each set of seismic observations. Each box identifies the region over which we averaged the flow vectors. Naturally, global convection models vary significantly based on input parameters such as viscosity, temperature, and among others. Our intent is not to investigate of full range of mantle flow scenarios but rather to provide a proof of concept of comparison between seismic anisotropy observations and global flow models near the CMB.

3. Results

3.1. VPSC-Based Elastic Tensor Library

Figure 4 displays a set of VPSC modeling results for 100% strain for simple shear, pure shear, and extensional scenarios for a series of modeled mineral and dominant slip system combinations that are tested in this study. The library includes calculated elastic tensors for the full suite of results, including a range of proposed single crystal elastic tensors, mixed phases, and various slip systems (see Tables S1–S17 in the supporting information). A subset of the library of elastic tensors with the predicted ScS, SKS, and SKKS shear wave splitting patterns for each of these models can be found in the supporting information (Figure S1). We find that the simple shear and pure shear tensors are generally very similar, except for a slight rotation in the overall pattern of anisotropy about the z axis. For extensional scenarios, the elastic tensor can be significantly different from the other strain geometries, but the strength of anisotropy is still high enough to be seismically observable. For all scenarios, ferropericlase yields the strongest anisotropy; however, the models displayed in Figure 4 are 100% by volume for each mineral. In the Earth, ferropericlase is only ~20% of the lower mantle.

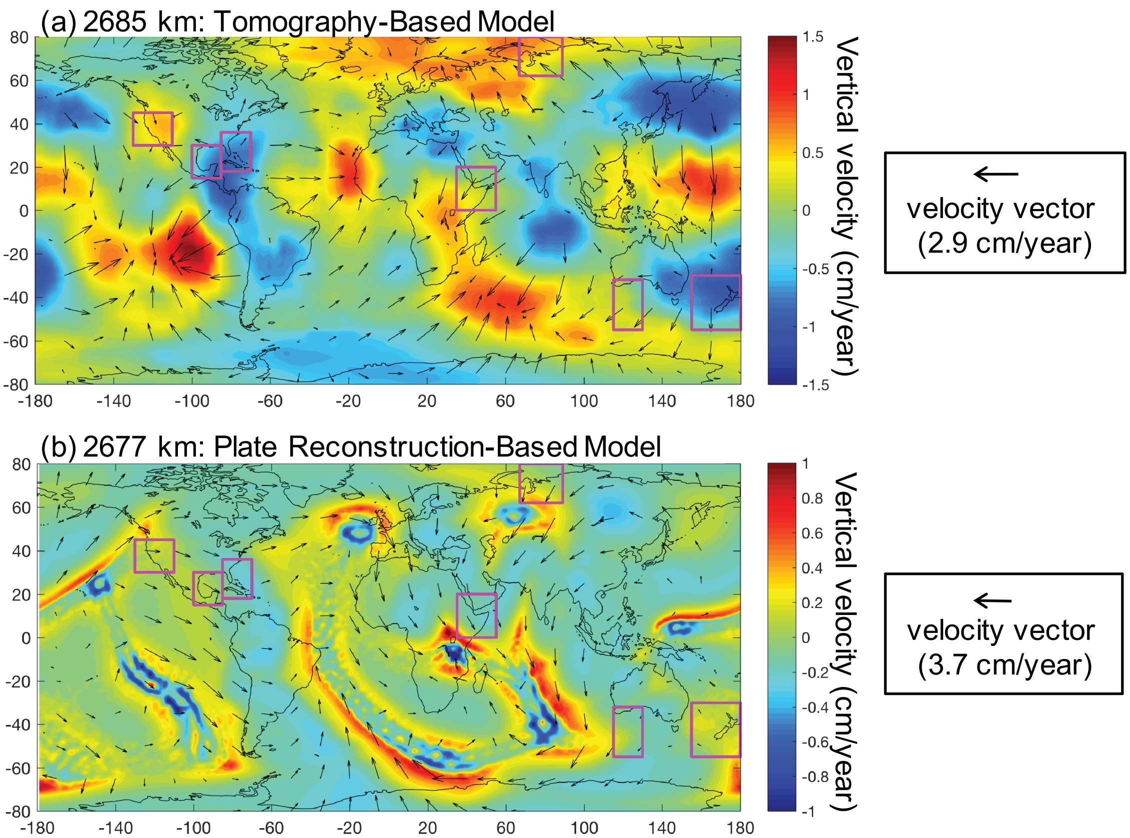

Figure 3. Global flow models examined in this study. Plots show predicted mantle flow in the vertical (color) and horizontal (arrows) directions just above the core-mantle boundary from two different studies: (a) Forte et al. (2015) at a depth of 2,685 km and (b) Flament (2019), at a depth of 2,677 km. Note the differences in scale between the two images: The vertical flow in (a) is approximately 1.5 times greater than (b), and horizontal flow in (b) is approximately 1.3 times greater than (a). Model in (a) is mostly based on global tomography models, while (b) does not include constraints from tomography but relies on plate reconstructions. Magenta boxes represent the regions of interest, over which we average the flow direction.

For most of the elastic tensors, the anisotropy is very similar to a vertical or slightly titled transverse isotropy pattern, in which (if the shear plane is parallel to the CMB) Vsh > Vsv for a horizontally propagating wave (similar to an S, ScS, or S_{diff} wave). The one exception to this observation may be for Ppv 2 and ferropericlase, where horizontal shear along the CMB could produce Vsv > Vsh, resulting in significant azimuthal anisotropy for horizontally propagating waves. For cases with a nonhorizontal shear plane, the elastic tensors could produce anisotropy that results in Vsv > Vsh for horizontally propagating waves.

We also explored the effect of the starting single crystal elastic tensor in our effective elastic tensor modeling. Figure 5 illustrates how important differences in single-crystal elastic constants can be when constructing an effective elastic tensor based on the VPSC polycrystalline modeled textures. In this example, we test four different candidate elastic tensors for Ppv at different pressures and temperatures. We find that the resulting effective elastic tensors are very similar for elasticity calculated at pressures less than 140 GPa and predict similar fast-axis direction and strength of anisotropy. However, for the high pressure (140 GPa) and high temperature (4,000 K) single-crystal elastic scenario, the overall strength of anisotropy is much weaker (by nearly 50–75%). The general pattern of fast-axis directions is similar to the other models in Figure 5, but the strength is quite different.

We also calculated a series of mixed-phase elasticity models for inclusion in the library. These models are calculated as simple, linear mixtures of different phases; elastic constants are calculated via weighted averages of the different phases. We emphasize that these mixed phase tensors are constructed from the VPSC modeling of texture development in each individual phase; our VPSC modeling scheme does not explicitly model polyphase deformation. For the mixed-phase models, we also explored a range of possible

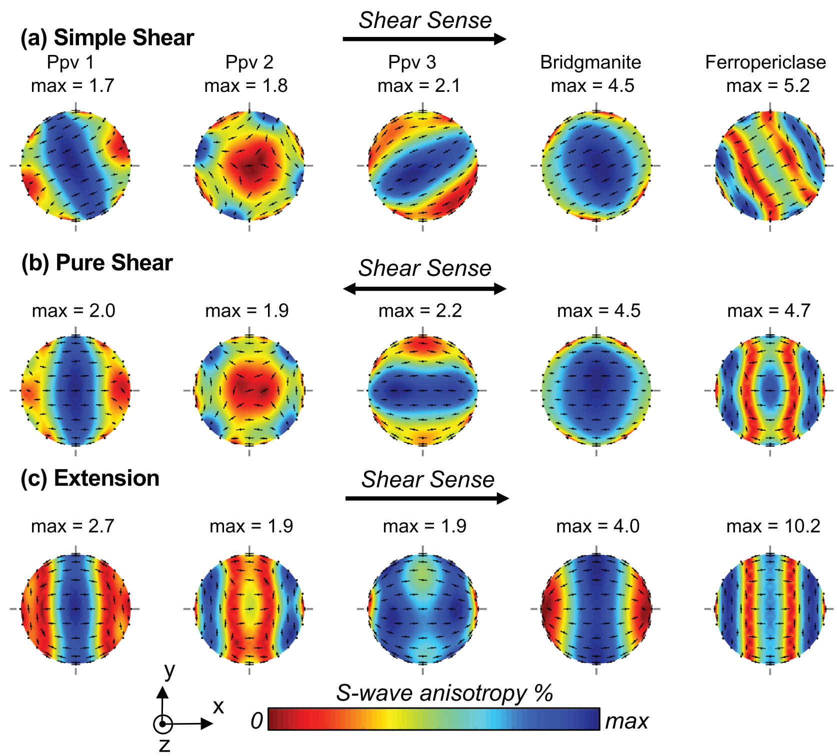

Figure 4. Stereoplots of *S* wave anisotropy predictions for a range of deformation geometries, candidate minerals, and slip systems. We show three deformation scenarios: (a) simple shear, (b) pure shear, and (c) extension. For each deformation geometry, we show results for Ppv for three different slip systems (Ppv 1: (010)<100>, Ppv 2: (001)<100>, Ppv 3: {011}<0–11> + (010)<100>), as well as bridgmanite and ferropericlase for the higher pressure slip systems listed in Table 1. Colors represent strength of anisotropy; color bars are not uniform, and instead, the maximum *S* wave anisotropy (%) is defined for each tensor. Coordinate system is displayed in the lower left. The shear direction is in the *x* direction (to the right) for simple shear and extension and in the positive and negative *x* direction for pure shear and the shear normal is in the *y* direction (upward).

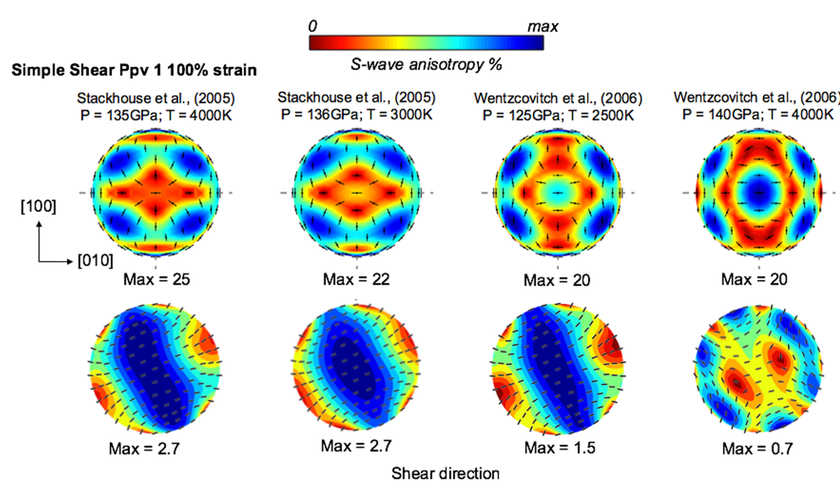

Figure 5. Comparison of elastic tensor predictions from VPSC modeling using different single-crystal elasticity estimates. We compare results using four different starting single-crystal elastic tensors (at 135 and 136 GPa from Stackhouse et al., 2005; at 125 and 140 GPa from Wentzcovitch et al., 2006). All models were calculated for the dominant slip system of Ppv 1, with simple shear and 100% strain. Colors represent strength of anisotropy, and the maximum *S* wave anisotropy (%) is defined for each tensor. Black bars represent fast splitting direction prediction in ray reference frame. Shear direction is to the right.

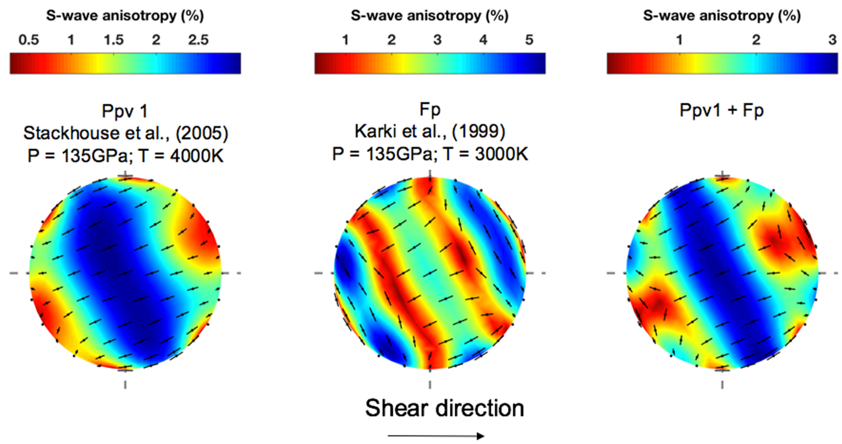

Figure 6. Comparison of shear wave splitting predictions for Ppv, Fp, and a mixed-phase tensor. We show results calculated for 100% strain and simple shear for pure postperovskite with the Ppv 1 slip systems (left), pure Fp with the higher pressure dominant slip plane (middle), and a mixed-phase model (right), with 25% Fp and 75% Ppv 1. Colors represent strength of anisotropy and the maximum *S* wave anisotropy (%) is shown for each tensor. Black bars represent fast splitting direction prediction in ray reference frame. Shear direction is to the right.

options for dominant slip system, strain geometry, shear orientation, and starting single crystal elasticity for bridgmanite, postperovskite, and ferropericlase. All models are listed in the supporting information as part of the library. Figure 6 illustrates an example of a simple shear scenario with a mixture of Ppv 1 and the higher-temperature dominant slip system for ferropericlase and the two phases mixed in a 75:25 mixture. In this example, postperovskite dominates the pattern of anisotropy, with a dominance of Vsh > Vsv for horizontally propagating waves.

3.2. Comparison of Results With Seismic Observations

Figure 7 illustrates an example of our forward modeling approach, which identifies every possible orientation of the ferropericlase elastic tensor that is consistent with the observations for two example data sets: Australia and western United States. In general, a combination of SKS, SKKS, and ScS observations can constrain the plausible orientations of an elastic tensor much more tightly than data sets that only include ScS shear wave splitting measurements (Creasy et al., 2019). This result makes the comparison between Australia and western United States interesting, because the western U.S. data set only includes ScS measurements while the Australia data set includes all phases. Overall, for the ScS-only case (western United States), we find that many orientations of the ferropericlase tensor could reproduce the data, as shown in Figure 7. However, for the Australia data set, the range of plausible orientations is much narrower. Figure 8 illustrates all possible solutions for each regional data set that combined SKS, SKKS, and ScS (Afar, Australia, and New Zealand) for a few selected models (ferropericlase and postperovskite). For the ScS-only data sets (Siberia and all North America data sets), there were many solutions that were possible; these solutions are demonstrated in the supporting information (Figure S2).

We ran our forward modeling scheme for each data set (Figure 2) for a range of elastic tensors associated with simple shear deformation geometries. When considering only these simple shear elastic tensors, we find that the observations in every regional data set considered here can be consistently reproduced with ferropericlase, Ppv 1, and Ppv 2, even accounting for both methods of using delay time. Bridgmanite can reproduce all of the ScS data sets, but none of the diverse data sets of SKS, SKKS, and ScS. Ppv 3 fits most of the data sets except Siberia and Australia.

In addition to testing the range of polycrystalline elastic tensors from our library, we also tested single-crystal elastic tensors against observations contained in each of these data sets. Elasticity scenarios based on single crystals are often used to model observations of shear wave splitting (e.g., Creasy et al., 2017; Ford et al., 2015); therefore, we wanted to compare how well a set of seismic observations fits both an elastic model based on a single crystal and its corresponding polycrystalline elastic tensor. For the ferropericlase single crystal, only the data sets of western United States and Caribbean are consistent with this elasticity

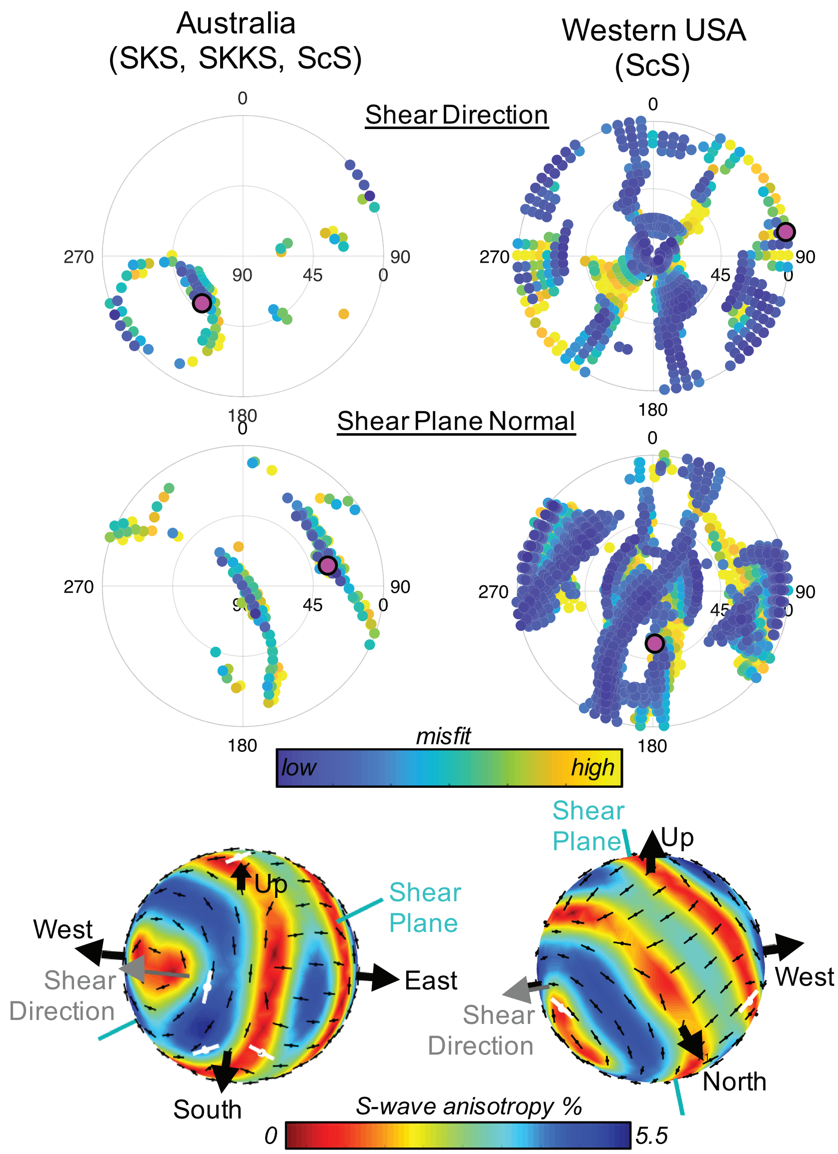

Figure 7. An example of our forward modeling results. In this example, we identify all possible orientations that fit the predictions of the elastic tensor describing simple shear of ferropericlase. Left panels: All possible solutions for the Australia data set (1 SKS, 1 SKKS, and 2 ScS measurements) for the shear direction (top stereonet) and the normal to the shear plane (middle stereonet), where colors represent a normalized misfit. Azimuth and inclination from the horizontal plane (represented in degrees) are plotted in an upper hemispherical projection relative to north (top of figure). The magenta point represents the orientation with the smallest misfit. Bottom image shows a stereoplot showing predicted *S* wave anisotropy for the best fitting orientations (same as magenta dot above) in which colors show *S* wave anisotropy (%) and black bars are predicted fast splitting directions. White bars show the actual splitting observations (Creasy et al., 2017) for comparison. Black arrows give geographic reference. Gray arrow indicates the shear direction, and the blue line indicates the shear plane normal. Right panels: Same as left panels, except we show results for the western U.S. data set (Nowacki et al., 2010), which includes two ScS paths. Note that the range of possible directions is much less tightly constrained than for the Australia data set.

tensor; in contrast, the polycrystalline VPSC ferropericlase tensor can fit every data set. However, the single-crystal elasticity of postperovskite from Wentzcovitch et al. (2006) behaves differently. This single crystal tensor, similar to the results of simple shear for Ppv 1 and Ppv 2 in the library, fits every single seismic data set as well. For bridgmanite, sometimes the single-crystal tensor fits a regional data set, but the polycrystalline bridgmanite does not, and vice versa. Therefore, bridgmanite and ferropericlase single crystals do not

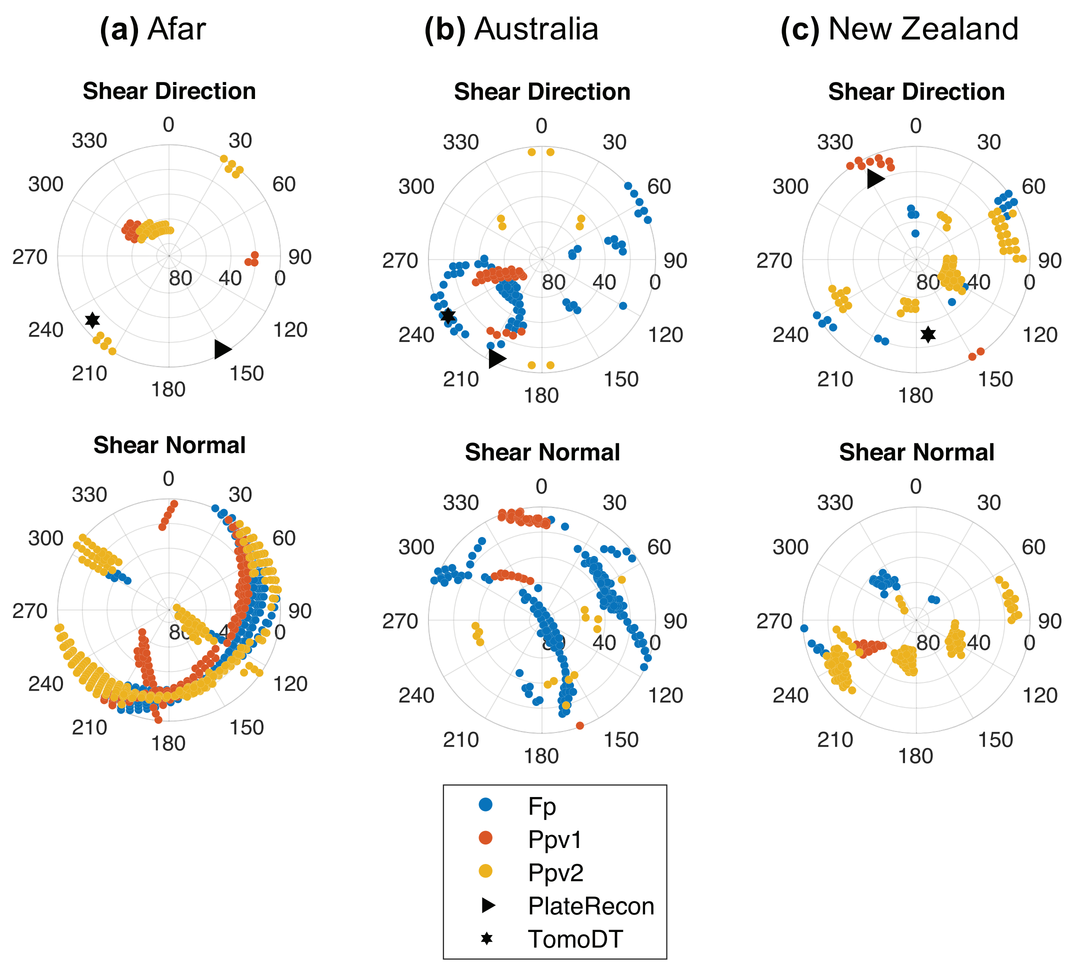

Figure 8. Modeling results for each data set that includes ScS, SKS, and SKKS: (a) Afar, (b) Australia, and (c) New Zealand. We show upper hemisphere stereoplots for all possible shear directions (top row) and shear plane normal (bottom row). Colors represent each candidate mineral or slip system. Only Fp and two slip systems for Ppv are shown, because these models were shown to be consistent with all regional observations in this study. For Afar, we used tensors calculated for the extensional strain geometry for 100% strain. For Australia and New Zealand, we used 100% strain and simple shear. Orientations of flow velocity vectors for each region from the flow models of PlateRecon of Flament (2019) and TomoDT of Forte et al. (2015) (see Figure 3) are shown on the upper row of plots with a black star and hexagram, respectively.

appear to be a fair approximation for their polycrystalline counterparts; in contrast, single-crystal postperovskite appears to fit the data just as well as Ppv 1 and Ppv 2 when considering relative delay times.

In addition to comparing the data sets to single crystals and pure endmember aggregate scenarios, we also compared the seismic observations to the simple shear, 100% strain, mixed scenarios for each of the proposed slip systems and models (75:25; bridgmanite/postperovskite: ferropericlase). Overall, we found that the mixed phases could reproduce the observations for each data set for all combinations of ferropericlase and slip system of Ppv. Interestingly, the mixture of bridgmanite and ferropericlase was able to find an acceptable fit to the data sets of Afar and Australia, while pure bridgmanite failed to fit either data set.

For the flow models shown in Figure 3, we compared the best fitting shear directions for all three deformation scenarios with the averaged flow vectors predicted by two different models, produced under different starting assumptions. Figure 9 shows the misfit between the closest acceptable orientation (for each regional data set) for a range of elastic tensors from our library and the average flow direction predicted by each flow model in the region of interest. The top three rows represent data sets that are diverse in terms of phases used (i.e., SKS, SKKS, and ScS), and the bottom four rows represent data sets that only include ScS splitting

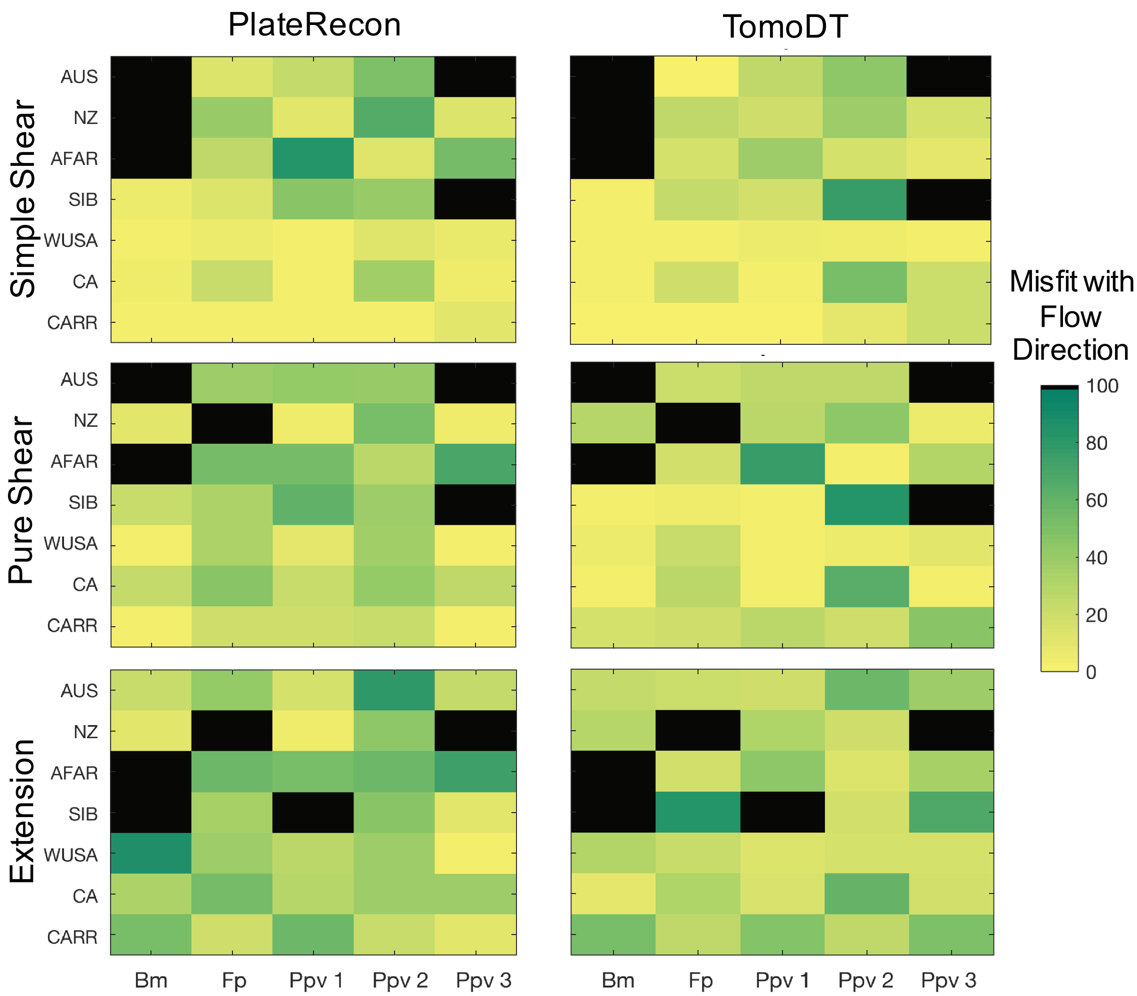

Figure 9. Misfit values are shown in color for each region and elastic tensor considered. Matrix of misfit values between best fitting anisotropy orientations and flow model predictions considered. We compared the closest acceptable shear direction for each candidate elastic tensor with the predicted flow direction from the plate reconstruction model of Flament (2019) in Figure 3b, left column, and the tomography-based model of Forte et al. (2015) in Figure 3a, right column. Forboxes shown in black, there was no acceptable solution for the given elastic tensor. AUS = Australia; NZ = New Zealand; AFAR = Afar plume; SIB = Siberia; WUSA = Western United States; CA = Central America; CARR = Caribbean. Bm = Bridgmanite; Fp = Ferropericlase; Ppv 1 = postperovskite (010)<100>; Ppv 2 = postperovskite (001)<100>; Ppv 3 = postperovskite {011}<0–11> + (010)<100>.

measurements. For simple shear (top row), the more diverse data sets result in the largest misfits with predicted flow direction, and the ScS data sets result in very small misfits. This discrepancy is a consequence of the fact that ScS-only data sets produce many more acceptable solutions than the diverse data sets (see Figure 7), and the plausible shear directions are therefore less well constrained. We caution, again, that directly comparing anisotropy and flow directions is a significant approximation; in future work, the development of finite strain will be explicitly taken into account.

4. Discussion

4.1. Regional Seismic Data Sets in the Context of New Elasticity Models: Implications for D''

Using the results from our forward modeling, we now investigate and interpret plausible mantle flow scenarios for each region of interest. We compare the inferences on plausible shear directions from our forward modeling to predictions from the global flow models, shown in Figure 3. Since Fp, Ppv 1, and Ppv 2 are the most consistently successful elasticity models across the range of regional data sets, we focus on those results. In general, we assume that simple shear is the most appropriate deformation geometry for D'', unless there is reason to consider other scenarios. For example, when slab remnants are present, it may be more appropriate to consider a pure compressional shear scenario, as might be expected for a slab impinging upon the CMB. When a plume may be present, vertical extension associated with upwelling may be more likely.

For the Australia data set, there is no specific evidence of slab material or deeply sourced plumes (Creasy et al., 2017), so we assume that simple shear is the likely deformation scenario here. We find that Ppv 1, Ppv 2, and Fp all fit the Australia observations very well, with a limited range of plausible shear directions. Both flow models (Figure 3) agree on generally horizontal flow to the southwest toward the edge of the African LLSVP beneath this region. The range of plausible shear directions for Fp and Ppv 1 includes shear directed toward the southwest, with a range of plausible angles from the horizontal (but including the possibility of horizontal shear). Ppv 2, however, does not include any possible shear directions toward the southwest; instead, shear direction is predicted to be north-south (horizontally inclined) or northwest/northeast (inclined by 45°). Overall, there are many plausible shear directions for these three mechanisms that include horizontal shear, either north-south or northeast-southwest (depending on the mechanism).

Beneath the New Zealand region, there is evidence for the presence of slab material, due to the very thick D'' layer (350 km, based on Usui et al., 2005), which may suggest colder temperatures, and the modeling of density anomalies with paleo subduction models (Steinberger, 2000). However, the two global models under consideration differ in the predicted flow direction (Figure 3). The tomography-based model predicts downwelling, mainly due to the fast anomalies observed in tomography models at the base of mantle beneath New Zealand (e.g., SAVANI, SEMUCB-WM1, and GyPSuM-S; Auer et al., 2014; French & Romanowicz, 2015; Simmons et al., 2010). However, the plate reconstruction model predicts modest upwelling. Therefore, it is somewhat difficult to predict the probable deformation scenario beneath New Zealand. If we assume simple shear, we find that Fp, Ppv 1, and Ppv 2 all permit plausible shear directions toward the south similar to that predicted by the tomography-based model (Figure 3a). If we assume pure shear (possibly due to subducting slab remnants impinging on the CMB), we find that Ppv 1 and Ppv 2 give reasonable shear directions, suggesting slightly inclined to near vertical flow (~40–80°). If there is upwelling as predicted by the plate reconstruction model, suggesting vertical extension, then Ppv 1 provides the smallest misfit between the best fitting shear orientation and the flow model prediction (Figure 9).

Beneath the Afar plume region, the data were collected near the edge of the African LLSVP. Many global tomography models have imaged the Afar plume from the CMB to the surface (e.g., SEMUCB-WM1 and S40RTS; French & Romanowicz, 2015; Ritsema et al., 2011), which might suggest upwelling flow. Interestingly, both flow models predict minimal upwelling and instead invoke mostly horizontally driven flow either to the southwest (Forte et al., 2015, in Figure 3a) or southeast (Flament, 2019, in Figure 3b) (Figure 8a). None of the plausible solutions identified through our forward modeling predict horizontally aligned shear directions, except Ppv 2, resulting in large discrepancies between predicted flow from the global models and the shear directions inferred from the forward modeling (Figure 9). Fp, Ppv 1, and Ppv 2 all predict highly inclined shear directions under an extensional regime (Figure 8a), consistent with a plume-like upwelling but inconsistent with mainly horizontal flow. However, sensitivity tests conducted on the flow model of Flament (2019: See their Figure 7) revealed that the flow regime near the edges of the LLSVPs is not very well constrained, so horizontal flow beneath Afar is far from certain. Our finding that the observations generally prefer flow scenarios that suggest upwelling beneath Afar are consistent with forward modeling results using single crystal-based elastic tensors, as discussed by Ford et al. (2015).

Beneath Siberia, the predictions of the two flow models differ greatly. Both flow models predict generally horizontally driven flow, but in different directions. The tomography-based model predicts flow toward the northwest (Forte et al., 2015, in Figure 3a), while the model of Flament (2019) in Figure 3b predicts flow to the south, toward the Perm anomaly (a relatively small low shear velocity anomaly in D'' beneath Russia; Lekic et al., 2012). It has been suggested that remnants of past subduction (80–130 Ma) are sinking and migrating to the west in this region (van der Meer et al., 2018), based on paleosubduction estimates. If we assume no change in flow for the past 100 Ma, then the model of Lithgow-Bertelloni and Richards (1998) predicts flow to the west-northwest, similar to the model of Forte et al. (2015) in Figure 3a. Two previous studies of D'' anisotropy in this region (Thomas et al., 2011; Wookey & Kendall, 2008) agree with this prediction of horizontal flow to the west-northwest, if deformation of postperovskite is assumed to be the mechanism. Based on our modeling with simple shear geometry, we find a range of possible shear directions for Fp, Ppv 1, and Ppv 2 elasticity models, but all of them are consistent with horizontal shear directions oriented toward the northwest. This result agrees with predictions based on the modeling of Kula plate subduction (Lithgow-Bertelloni & Richards, 1998) and with the flow model predictions of Forte et al. (2015; Figure 3a). For each of the elasticity models (Fp, Ppv 1, and Ppv 2), we found that inclined (anywhere from 0° to 90° from the horizontal for simple shear scenarios) flow toward the south is also possible, which would be consistent with the flow model predictions of Flament (2019).

Beneath the western U.S. region, seismic anisotropy has been identified near the edge of the Pacific LLSVP (Nowacki et al., 2010). The flow model of Forte et al. (2015) in Figure 3a predicts slight upwelling, and the flow model of Flament (2019) in Figure 3b predicts generally horizontal flow toward the east-southeast. Nowacki et al. (2010) interpreted their ScS splitting measurements in the context of flow to either the southeast or northwest, induced by subduction of the Farallon slab beneath North America. Elastic tensor models calculated under simple shear for Fp, Ppv 1, and Ppv 2, when compared against observations, predict plausible shear orientations that include directions predicted by both global flow models. We note, however, that there are many possible shear directions that fit this data set, due to the nonuniqueness of forward modeling only ScS shear wave splitting measurements over just two paths. Due to this nonuniqueness, we also cannot eliminate other possibilities for shear directions for this region. For this reason, the misfits between flow predictions and the closest acceptable shear direction are very small in Figure 9. Our results for the western United States illustrate the difficulty inherent in modeling D″ anisotropy when a small number of raypaths is used (e.g., Creasy et al., 2019).

Beneath Central America and the Caribbean region, remnants of the Farallon slab are potentially present within the lower mantle (van der Meer et al., 2018). These remnants may be inducing either simple or pure shear associated with downwelling in this region. The model of Forte et al. (2015) predicts strong downwelling here (Figure 3a), but Flament (2019) predicts horizontal flow toward the southeast (Figure 3b). We used both simple shear and pure shear tensors to model observations beneath this region. We found that Ppv 1, for either simple or pure shear, produces the smallest misfit between flow predictions and plausible shear directions for both of the flow models. Elasticity models based on Fp and Ppv 2 have larger misfits. Interestingly, the forward modeling conducted by Nowacki et al. (2010) yielded a preferred model consistent with our Ppv 2 model but also found acceptable solutions for slip on (010)—our Ppv 1 model.

Overall, our modeling results show that each of the three most likely anisotropy scenarios (Fp, Ppv 1, and Ppv 2) yield geodynamically plausible estimates for shear directions. However, given the large differences in predicted flow directions between the two flow models considered for several of the regions under study, we cannot say whether one of these scenarios should be preferred over the others. This modeling exercise illuminates some of the challenges in modeling of *D*″ anisotropy data sets, as their interpretation in terms of flow are usually nonunique. Despite the challenges, however, we have demonstrated that the tools are in place to test whether the predictions of a given geodynamic flow model are consistent with observations of *D*″ anisotropy.

4.2. Implications for Future Studies of *D*″ Anisotropy

We have developed a set of plausible elastic tensors calculated for endmember deformation scenarios for a range of likely candidate mechanisms (minerals and dominant slip systems) for *D*″ anisotropy, resulting in a library of 336 elastic tensors. Simple and pure shear is likely to be the most common deformation geometries in the lowermost mantle, as it is a horizontal boundary layer where subducting slabs may drive flow (e.g., Wenk et al., 2011). Extensional scenarios could be possible at the base of an upwelling, where material is extended along the plume (e.g., Tommasi et al., 2018). Based on our comparisons between plausible elastic tensor scenarios and available observational data sets, we find that Fp, Ppv 1, and Ppv 2 are the most likely candidate mechanisms for *D*″ anisotropy, as they fit all of the available data sets. Bridgmanite also provides a reasonable fit to data sets that are limited to ScS measurements only, but data sets that include a range of different data types (ScS, SKS, and SKKS splitting) are not well reproduced with bridgmanite elasticity models. Ppv 3 fails to fit only the Australia and Siberia data sets for simple and pure shear. Our modeling results provide additional support to the idea that ScS shear wave splitting observations alone provide relatively weak constraints on anisotropy geometry, but combining ScS with SKS and SKKS splitting observations dramatically removes the range of possible models that can fit the data (Creasy et al., 2019). Of course, ScS shear wave splitting data sets do provide significant contributions to our understanding of possible flow directions in *D*″ if the mechanism for anisotropy is known or assumed.

Even though we found that the available body wave data sets could not uniquely constrain a single mechanism for anisotropy, our finding that bridgmanite and one particular slip system of postperovskite (Ppv 3) provide generally poorer fits to the observations is significant. Bridgmanite is the most abundant mineral in the bulk of the lower mantle, but available shear wave splitting data sets are not generally consistent with textured bridgmanite. This result likely implies that in regions of D'' that exhibit anisotropy, bridgmanite has undergone a phase transition to Ppv, and the D'' layer is dominated by Ppv undergoing deformation in the dislocation creep regime. Ferropericlase remains a plausible mechanism for D'' anisotropy, but it has proven difficult to model in past studies, since the single-crystal elasticity of ferropericlase is significantly different in its geometry from its polycrystalline counterpart. We found that two dominant slip systems for postperovskite on the (010) (Ppv 1) and (001) (Ppv 2) planes are plausible mechanisms for D'' anisotropy, while the third (Ppv 3; {011}<0–11> + (010)<100>) is less likely.

4.3. Caveats and Future Work

We reiterate that we have made several assumptions in our modeling framework, and reexamining some of these assumptions may provide fruitful avenues for future work. First, we assumed ray theory in all of our forward modeling; moving to a full-wave framework will be a necessary step for future studies (e.g., Nowacki & Wookey, 2016). Second, we compared our shear direction estimates to local velocity values from the global flow models rather than explicitly calculating estimates of finite strain. More detailed studies that calculate the finite strain evolution for global flow models are needed in the future. Third, there are many potential mineralogical complications that we did not incorporate. Specifically, we did not consider possible effects of impurities of Fe and Al on the elasticity of bridgmanite, postperovskite, or ferropericlase. To highlight one example, the presence of iron appears to increase the anisotropic strength of ferropericlase (Finkelstein et al., 2018; Marquardt et al., 2009).

A fourth set of assumptions in our work is that we only considered single phases or simple mixtures of phases in this study. In reality, the lower mantle consists of multiple phases deforming together. Future work will have to consider the complications of deforming multiphase aggregates. Some experimental evidence has shown that ferropericlase does not deform in a coherent texture when deformed with bridgmanite in a diamond anvil cell (Miyagi & Wenk, 2016). Ferropericlase is much weaker than bridgmanite, but postperovskite has a similar strength or is even weaker than ferropericlase at D'' conditions (Ammann et al., 2010; Romanowicz & Wenk, 2017). Therefore, additional effort is needed to determine the appropriate elastic tensors for polyphase mixtures such as postperovskite and ferropericlase or bridgmanite and ferropericlase.

Despite the assumptions made here, our first-order global comparison results in some important insight into flow at the base of the mantle, as discussed in sections 4.1 and 4.2. As observational studies of D'' anisotropy continue to mature, we hope that the elastic tensor library presented here will facilitate the interpretation of observations in terms of mantle flow. While currently available body wave data sets are generally insufficient for fully constraining a unique elastic tensor, we see avenues for progress in future comparisons between flow models and D'' anisotropy observations. As demonstrated in this study and by Creasy et al. (2019), the simultaneous interpretation of diverse data sets including the splitting of phases such as ScS, SKS, SKKS, Sdiff, PKS, and PcS reflections from the D'' interface and normal modes can lead to more tightly constrained models for D'' anisotropy. The elastic tensor library presented in this study can provide a framework for linking observations of D'' to insights about mantle flow.

5. Conclusions

We have developed a VPSC-based elastic tensor library for lower mantle anisotropy scenarios, based on a range of candidate minerals and deformation geometries. We considered five likely mechanisms for lowermost mantle anisotropy, invoking dislocation creep in bridgmanite, ferropericlase, and postperovskite considering different candidate dominant slip systems. We compared predictions based on this elastic tensor library to previously published shear wave splitting observations due to anisotropy in the D'' layer. These comparisons demonstrate that ferropericlase and postperovskite make predictions that are most consistent with the observations of D'' anisotropy, although the data cannot uniquely distinguish between these two mechanisms. Bridgmanite is the least probable mechanism. In general, the shear directions (see Figure 9) inferred for the ferropericlase and postperovskite elasticity models agree with the model predictions for present-day flow within the D'' layer (Flament, 2019; Forte et al., 2015), except for the Afar region.

Our elastic tensor library will enable future studies to compare predictions of flow in the lowermost mantle directly to seismic anisotropy measurements and will provide a set of plausible interpretative schema for D'' anisotropy observations. With improved frameworks for interpretation, such observations will continue to advance our ability to evaluate models of mantle convection and infer flow at the base of the mantle. We hope the elastic tensor library enables the collaboration among seismologists, mineral physicists, and geodynamicists to fully engage this problem by making full use of anisotropy observations to understand the dynamics of the lowermost mantle.

Acknowledgments
This work was supported by a National Science Foundation (NSF) Graduate Research Fellowship Grant DGE-1122492 to N. C. and by NSF Grant EAR-1547499 to M. D. L. We thank the Yale Center for Research Computing for guidance and use of the research computing infrastructure. We thank A. M. Forte and N. Flament for providing flow models for this study and for useful discussions. This study was initiated at the 2018 Cooperative Institute for Dynamic Earth Research (CIDER) summer program. CIDER-II is funded as a "Synthesis Center" by the Frontiers of Earth Systems Dynamics (FESD) program of NSF under Grant EAR-1135452. Seismic data sets for this research were found in Wookey and Kendall (20082008), Nowacki et al. (20102010), Ford et al. (20152015), and Creasy et al. (20172017). CRSS values for this research were found in Immoor et al. (20182018), Lin et al. (20192019), Couper et al. (20182018), and Miyagi and Wenk (20162016). All results (elastic tensor library) produced in this study are included in the supporting information and were calculated using VPSC Version 6 (Lebensohn & Tomé, 19941994). The supporting information is available in a Mendeley repository (https://doi.org/10.17632/4g74ckz6k2.1). We thank Sarah Brownlee and an associate editor for constructive comments that helped to improve the paper.

References

Ammann, M. W., Brodholt, J. P., Wookey, J., & Dobson, D. P. (2010). First-principles constraints on diffusion in lower-mantle minerals and a weak D′′ layer. *Nature*, *465*(7297), 462–465. https://doi.org/10.1038/nature09052

Amodeo, J., Carrez, P., & Cordier, P. (2012). Modelling the effect of pressure on the critical shear stress of MgO single crystals. *Philosophical Magazine*, *92*, 1523–1541. https://doi.org/10.1080/14786435.2011.652689

Auer, L., Boschi, L., Becker, T. W., Nissen-Meyer, T., & Giardini, D. (2014). Savani: A variable resolution whole-mantle model of anisotropic shear velocity variations based on multiple data sets. *Journal of Geophysical Research - Solid Earth*, *119*, 3006–3034. https://doi.org/10.1002/2013JB010773

Caracas, R. (2010). Elasticity of AlFeO3 and FeAlO3 perovskite and post-perovskite from first-principles calculations. *Geophysical Research Letters*, *37*, L20306. https://doi.org/10.1029/2010GL044404

Chevrot, S. (2000). Multichannel analysis of shear wave splitting. *Journal of Geophysical Research*, *105*, 21,579–21,590. https://doi.org/10.1029/2000JB900199

Cordier, P., Amodeo, J., & Carrez, P. (2012). Modelling the rheology of MgO under Earth's mantle pressure, temperature and strain rates. *Nature*, *481*(7380), 177–180. https://doi.org/10.1038/nature10687

Cottaar, S., Li, M., McNamara, A. K., Romanowicz, B., & Wenk, H.-R. (2014). Synthetic seismic anisotropy models within a slab impinging on the core-mantle boundary. *Geophysical Journal International*, *199*, 164–177. https://doi.org/10.1093/gji/ggu244

Cottaar, S., & Romanowicz, B. (2013). Observations of changing anisotropy across the southern margin of the African LLSVP. *Geophysical Journal International*, *195*(2), 1184–1195. https://doi.org/10.1093/gji/ggt285

Couper S., Speziale S., Marquardt H., Liermann H.P., Miyagi L., 2018. Texture development and slip system activities of bridgmanite during high temperature deformation of a lower mantle assemblage in a resistively heated diamond anvil cell, 2018 Fall Meeting, AGU, Washington, DC.

Creasy, N., Long, M. D., & Ford, H. A. (2017). Deformation in the lowermost mantle beneath Australia from observations and models of seismic anisotropy. *Journal of Geophysical Research - Solid Earth*, *122*, 5243–5267. https://doi.org/10.1002/2016JB013901

Creasy, N., Pisconti, A., Long, M. D., Thomas, C., & Wookey, J. (2019). Constraining lowermost mantle anisotropy with body waves: A synthetic modelling study. *Geophysical Journal International*, *217*, 766–783. https://doi.org/10.1093/gji/ggz049

Crotwell, H. P., Owens, T. J., & Ritsema, J. (1999). The TauP toolkit: Flexible seismic travel-time and ray-path utilities. *Seismological Research Letters*, *70*, 154–160. https://doi.org/10.1785/gssrl.70.2.154

Faccenda, M. (2014). Mid mantle seismic anisotropy around subduction zones. *Physics of the Earth and Planetary Interiors*, *227*, 1–19. https://doi.org/10.1016/j.pepi.2013.11.015

Finkelstein, G. J., Jackson, J. M., Said, A., Alatas, A., Leu, B. M., Sturhahn, W., & Toellner, T. S. (2018). Strongly anisotropic magnesiowüstite in Earth's lower mantle. *Journal of Geophysical Research - Solid Earth*, *123*, 4740–4750. https://doi.org/10.1029/2017JB015349

Flament, N. (2019). Present-day dynamic topography and lower-mantle structure from palaeogeographically constrained mantle flow models. *Geophysical Journal International*, *216*, 2158–2182. https://doi.org/10.1093/gji/ggy526

Ford, H. A., Long, M. D., He, X., & Lynner, C. (2015). Lowermost mantle flow at the eastern edge of the African large low shear velocity province. *Earth and Planetary Science Letters*, *420*, 12–22. https://doi.org/10.1016/j.epsl.2015.03.029

Forte, A. M., Simmons, N. A., & Grand, S. P. (2015). Constraints on seismic models from other disciplines—Implications for the global mantle convective flow. In B. Romanowicz, & A. M. Dziewonski (Eds.), *Volume 1 of Treatise of Geophysics*, (2nd ed. pp. 853–907). Amsterdam, Netherlands: Elsevier.

French, S. W., & Romanowicz, B. (2015). Broad plumes rooted at the base of the Earth's mantle beneath major hotspots. *Nature*, *525*(7567), 95–99. https://doi.org/10.1038/nature14876

Girard, J., Chen, J., & Raterron, P. (2012). Deformation of periclase single crystals at high pressure and temperature: Quantification of the effect of pressure on slip-system activities. *Journal of Applied Physics*, *111*, 112,607. https://doi.org/10.1063/1.4726200

He, X., & Long, M. D. (2011). Lowermost mantle anisotropy beneath the northwestern Pacific: Evidence from PcS, ScS, SKS, and SKKS phases. *Geochemistry, Geophysics, Geosystems*, *12*, Q12012. https://doi.org/10.1029/2011GC003779

Hirose, K., Nagaya, Y., Merkel, S., & Ohishi, Y. (2010). Deformation of MnGeO $_3$ post-perovskite at lower mantle pressure and temperature: High P-T deformation of post-perovskite. *Geophysical Research Letters*, *37*, L20302. https://doi.org/10.1029/2010GL044977

Immoor, J., Marquardt, H., Miyagi, L., Lin, F., Speziale, S., Merkel, S., et al. (2018). Evidence for {100}<011> slip in ferropericlase in Earth's lower mantle from high-pressure/high-temperature experiments. *Earth and Planetary Science Letters*, *489*, 251–257. https://doi.org/10.1016/j.epsl.2018.02.045

Karato, S. I. (2008). Deformation of earth materials. In *An Introduction to the Rheology of Solid Earth* (Chap. 9, Vol. 463). New York, USA: Cambridge University Pres.

Karki, B. B., Wentzcovitch, R. M., de Gironcoli, S., & Baroni, S. (1999). First-principles determination of elastic anisotropy and wave velocities of MgO at lower mantle conditions. *Science*, *286*(5445), 1705–1707. https://doi.org/10.1126/science.286.5445.1705

Kendall, J.-M., & Shearer, P. M. (1994). Lateral variations in D'' thickness from long-period shear wave data. *Journal of Geophysical Research*, *99*, 11,575–11,590. https://doi.org/10.1029/94JB00236

Kennett, B. L. N., Engdahl, E. R., & Buland, R. (1995). Constraints on seismic velocities in the Earth from traveltimes. *Geophysical Journal International*, *122*, 108–124. https://doi.org/10.1111/j.1365-246X.1995.tb03540.x

Kubo, A., Kiefer, B., Shim, S.-H., Shen, G., Prakapenka, V. B., & Duffy, T. S. (2008). Rietveld structure refinement of MgGeO3 post-perovskite phase to 1 Mbar. *American Mineralogist*, *93*, 965–976. https://doi.org/10.2138/am.2008.2691

Lay, T., & Helmberger, D. V. (1983). The shear-wave velocity gradient at the base of the mantle. *Journal of Geophysical Research*, *88*, 8160–8170. https://doi.org/10.1029/JB088iB10p08160

Lay, T., & Young, C. J. (1991). Analysis of seismic SV waves in the core's penumbra. *Geophysical Research Letters*, *18*, 1373–1376. https://doi.org/10.1029/91GL01691

Lebensohn, R. A., Castañeda, P. P., Brenner, R., & Castelnau, O. (2011). Full-field vs. homogenization methods to predict microstructure-property relations for polycrystalline materials. In S. Ghosh, & D. Dimiduk (Eds.), *Computational methods for microstructure-property relationships*, (pp. 393–441). Boston, MA: Springer US. https://doi.org/10.1007/978-1-4419-0643-4_11

Lebensohn, R. A., & Tomé, C. N. (1994). A self-consistent viscoplastic model: Prediction of rolling textures of anisotropic polycrystals. *Materials Science and Engineering A*, *175*, 71–82. https://doi.org/10.1016/0921-5093(94)91047-2

Lee, K. K. M., O'Neill, B., Panero, W. R., Shim, S.-H., Benedetti, L. R., & Jeanloz, R. (2004). Equations of state of the high-pressure phases of a natural peridotite and implications for the Earth's lower mantle. *Earth and Planetary Science Letters*, *223*, 381–393. https://doi.org/10.1016/j.epsl.2004.04.033

Lekic, V., Cottaar, S., Dziewonski, A., & Romanowicz, B. (2012). Cluster analysis of global lower mantle tomography: A new class of structure and implications for chemical heterogeneity. *Earth and Planetary Science Letters*, *357–358*, 68–77. https://doi.org/10.1016/j.epsl.2012.09.014

Lin, F., Couper, S., Jugle, M., & Miyagi, L. (2019). Competing deformation mechanisms in periclase: Implications for lower mantle anisotropy. *Minerals*, *9*, 650.

Lin, F., Hilairet, N., Raterron, P., Addad, A., Immoor, J., Marquardt, H., et al. (2017). Elasto-Viscoplastic Self Consistent (EVPSC) modeling of the ambient temperature plastic behavior of periclase deformed up to 5.4 GPa. *Journal of Applied Physics*, *122*, 205902. https://doi.org/10.1063/1.4999951

Lin, F., Miyagi L., (2017). Modeling lattice strain and texture in post-perovskite phases: Implications for slip system activity, *2017 Stewardship Science Academic Program,* Naperville, IL.

Lithgow-Bertelloni, C., & Richards, M. A. (1998). The dynamics of Cenozoic and Mesozoic plate motions. *Reviews of Geophysics*, *36*, 27–78. https://doi.org/10.1029/97RG02282

Long, M. D., & Becker, T. W. (2010). Mantle dynamics and seismic anisotropy. *Earth and Planetary Science Letters*, *297*, 341–354. https://doi.org/10.1016/j.epsl.2010.06.036

Lynner, C., & Long, M. D. (2014a). Sub-slab anisotropy beneath the Sumatra and circum-Pacific subduction zones from source-side shear wave splitting observations. *Geochemistry, Geophysics, Geosystems*, *15*, 2262–2281. https://doi.org/10.1002/2014GC005239

Lynner, C., & Long, M. D. (2014b). Lowermost mantle anisotropy and deformation along the boundary of the African LLSVP. *Geophysical Research Letters*, *41*, 3447–3454. https://doi.org/10.1002/2014GL059875

Marquardt, H., Speziale, S., Reichmann, H. J., Frost, D. J., Schilling, F. R., & Garnero, E. J. (2009). Elastic shear anisotropy of Ferropericlase in Earth's lower mantle. *Science*, *324*(5924), 224–226. https://doi.org/10.1126/science.1169365

Matthies, S., & Humbert, M. (1993). The realization of the concept of a geometric mean for calculating physical constants of polycrystalline materials. Phys. *Status Solidi B*, *177*, K47–K50. https://doi.org/10.1002/pssb.2221770231

Maupin, V. (1994). On the possibility of anisotropy in the *D″* layer as inferred from the polarization of diffracted S waves. *Physics of the Earth and Planetary Interiors*, *87*, 1–32. https://doi.org/10.1016/0031-9201(94)90019-1

Merkel, S., Kubo, A., Miyagi, L., Speziale, S., Duffy, T. S., Mao, H., & Wenk, H.-R. (2006). Plastic deformation of MgGeO3 post-perovskite at lower mantle pressures. *Science*, *311*(5761), 644–646. https://doi.org/10.1126/science.1121808

Merkel, S., McNamara, A. K., Kubo, A., Speziale, S., Miyagi, L., Meng, Y., et al. (2007). Deformation of (Mg,Fe)SiO3 post-perovskite and "*D*" anisotropy. *Science*, *316*(5832), 1729–1732. https://doi.org/10.1126/science.1140609

Merkel, S., Wenk, H. R., Shu, J., Shen, G., Gillet, P., Mao, H., & Hemley, R. J. (2002). Deformation of polycrystalline MgO at pressures of the lower mantle. *Journal of Geophysical Research*, *107*(B11), 2271. https://doi.org/10.1029/2001JB000920

Mitrovica, J. X., & Forte, A. M. (2004). A new inference of mantle viscosity based upon joint inversion of convection and glacial isostatic adjustment data. *Earth and Planetary Science Letters*, *225*, 177–189. https://doi.org/10.1016/j.epsl.2004.06.005

Miyagi, L., Kanitpanyacharoen, W., Kaercher, P., Lee, K. K. M., & Wenk, H.-R. (2010). Slip systems in MgSiO3 post-perovskite: Implications for *D′′* anisotropy. *Science*, *329*(5999), 1639–1641. https://doi.org/10.1126/science.1192465

Miyagi, L., Kanitpanyacharoen, W., Stackhouse, S., Militzer, B., & Wenk, H.-R. (2011). The enigma of post-perovskite anisotropy: Deformation versus transformation textures. *Physics and Chemistry of Minerals*, *38*(9), 665–678. https://doi.org/10.1007/s00269-011-0439-y

Miyagi, L., Nishiyama, N., Wang, Y., Kubo, A., West, D. V., Cava, R. J., et al. (2008). Deformation and texture development in CaIrO3 post-perovskite phase up to 6 GPa and 1300 K. *Earth and Planetary Science Letters*, *268*, 515–525. https://doi.org/10.1016/j.epsl.2008.02.005

Miyagi, L., & Wenk, H.-R. (2016). Texture development and slip systems in bridgmanite and bridgmanite + ferropericlase aggregates. *Physics and Chemistry of Minerals*, *43*(8), 597–613. https://doi.org/10.1007/s00269-016-0820-y

Murakami, M., Hirose, K., Kawamura, K., Sata, N., & Ohishi, Y. (2004). Post-perovskite phase transition in MgSiO3. *Science*, *304*(5672), 855–858. https://doi.org/10.1126/science.1095932

Nowacki, A., & Wookey, J. (2016). The limits of ray theory when measuring shear wave splitting in the lowermost mantle with ScS waves. *Geophysical Journal International*, *207*, 1573–1583. https://doi.org/10.1093/gji/ggw358

Nowacki, A., Wookey, J., & Kendall, J. M. (2010). Deformation of the lowermost mantle from seismic anisotropy. *Nature*, *467*(7319), 1091–1094. https://doi.org/10.1038/nature09507

Nowacki, A., Wookey, J., & Kendall, J. M. (2011). New advances in using seismic anisotropy, mineral physics and geodynamics to understand deformation in the lowermost mantle. *Journal of Geodynamics*, *52*, 205–228. https://doi.org/10.1016/j.jog.2011.04.003

Okada, T., Yagi, T., Niwa, K., & Kikegawa, T. (2010). Lattice-preferred orientations in post-perovskite-type MgGeO3 formed by transformations from different pre-phases. *Physics of the Earth and Planetary Interiors*, *180*, 195–202. https://doi.org/10.1016/j.pepi.2009.08.002

Ritsema, J., Deuss, A., van Heijst, H. J., & Woodhouse, J. H. (2011). S40RTS: A degree-40 shear-velocity model for the mantle from new Rayleigh wave dispersion, teleseismic traveltime and normal-mode splitting function measurements. *Geophysical Journal International*, *184*, 1223–1236. https://doi.org/10.1111/j.1365-246X.2010.04884.x

10.1029/2019GC008883

Romanowicz, B., & Wenk, H.-R. (2017). Anisotropy in the deep Earth. *Physics of the Earth and Planetary Interiors*, *269*, 58–90. https://doi.org/10.1016/j.pepi.2017.05.005

Savage, M. K. (1999). Seismic anisotropy and mantle deformation: What have we learned from shear wave splitting? *Reviews of Geophysics*, *37*, 65–106. https://doi.org/10.1029/98RG02075

Simmons, N. A., Forte, A. M., Boschi, L., & Grand, S. P. (2010). GyPSuM: A joint tomographic model of mantle density and seismic wave speeds. *Journal of Geophysical Research*, *115*, B12310. https://doi.org/10.1029/2010JB007631

Stackhouse, S., Brodholt, J. P., Wookey, J., Kendall, J.-M., & Price, G. D. (2005). The effect of temperature on the seismic anisotropy of the perovskite and post-perovskite polymorphs of MgSiO3. *Earth and Planetary Science Letters*, *230*, 1–10. https://doi.org/10.1016/j.epsl.2004.11.021

Steinberger, B. (2000). Slabs in the lower mantle—results of dynamic modelling compared with tomographic images and the geoid. *Physics of the Earth and Planetary Interiors*, *118*(3-4), 241–257.

Stretton, I., Heidelbach, F., Mackwell, S., & Langenhorst, F. (2001). Dislocation creep of magnesiowüstite (Mg0. 8Fe0. 2O). *Earth and Planetary Science Letters*, *194*(1–2), 229–240.

Thomas, C., Wookey, J., Brodholt, J., & Fieseler, T. (2011). Anisotropy as cause for polarity reversals of D″reflections. *Earth and Planetary Science Letters*, *307*(3-4), 3697–376.

Tome, D. N., & Canova, G. R. (2000). Self-consistent mdoeling of heterogenous plasticity. In U. F. Kocks, C. N. Tome, & H. F. Wenk (Eds.), *texture and anistropy. Preferred orientations in polycrystals and their effect on materials properties*, (2nd ed.pp. 466–510). Cambridge, UK: Cambridge Univ press.

Tommasi, A., Goryaeva, A., Carrez, P., Cordier, P., & Mainprice, D. (2018). Deformation, crystal preferred orientations, and seismic anisotropy in the Earth's *D*″ layer. *Earth and Planetary Science Letters*, *492*, 35–46. https://doi.org/10.1016/j.epsl.2018.03.032

Tsujino, N., Nishihara, Y., Yamazaki, D., Seto, Y., Higo, Y., & Takahashi, E. (2016). Mantle dynamics inferred from the crystallographic preferred orientation of bridgmanite. *Nature*, *539*(7627), 81–84. https://doi.org/10.1038/nature19777

Usui, Y., Hiramatsu, Y., Furumoto, M., & Kanao, M. (2005). Thick and anisotropic *D*″ layer beneath Antarctic Ocean. *Geophysical Research Letters*, *32*, L13311. https://doi.org/10.1029/2005GL022622

van der Meer, D. G., van Hinsbergen, D. J. J., & Spakman, W. (2018). Atlas of the underworld: Slab remnants in the mantle, their sinking history, and a new outlook on lower mantle viscosity. *Tectonophysics*, *723*, 309–448. https://doi.org/10.1016/j.tecto.2017.10.004

Vinnik, L., Romanowicz, B., Stunff, Y. L., & Makeyeva, L. (1995). Seismic anisotropy in the *D*″ layer. *Geophysical Research Letters*, *22*, 1657–1660. https://doi.org/10.1029/95GL01327

Walker, A. M., Forte, A. M., Wookey, J., Nowacki, A., & Kendall, J.-M. (2011). Elastic anisotropy of *D*″ predicted from global models of mantle flow. *Geochemistry, Geophysics, Geosystems*, *12*, Q10006. https://doi.org/10.1029/2011GC003732

Walker, A. M., & Wookey, J. (2012). MSAT—A new toolkit for the analysis of elastic and seismic anisotropy. *Computational Geosciences*, *49*, 81–90. https://doi.org/10.1016/j.cageo.2012.05.031

Wang, H., Wu, P. D., Tomé, C. N., & Huang, Y. (2010). A finite strain elastic–viscoplastic self-consistent model for polycrystalline materials. *Journal of the Mechanics and Physics of Solids*, *58*(4), 594–612.

Weber, M., & Davis, J. P. (1990). Evidence of a laterally variable lower mantle structure from P- and S-waves. *Geophysical Journal International*, *102*, 231–255. https://doi.org/10.1111/j.1365-246X.1990.tb00544.x

Wenk, H. R. (2000). Pole figure measurements with diffraction techniques. In U. F. Kocks, C. N. Tome, & H. F. Wenk (Eds.), *Texture and anistropy. Preferred orientations in polycrystals and their effect on materials properties*, (2nd ed.pp. 127–177). Cambridge, UK: Cambridge Univ press.

Wenk, H. R., Cottaar, S., Tomé, C. N., McNamara, A., & Romanowicz, B. (2011). Deformation in the lowermost mantle: From polycrystal plasticity to seismic anisotropy. *Earth and Planetary Science Letters*, *306*, 33–45. https://doi.org/10.1016/j.epsl.2011.03.021

Wenk, H. R., Matthies, S., Donovan, J., & Chateigner, D. (1998). BEARTEX: A windows-based program system for quantitative texture analysis. *Journal of Applied Crystallography*, *31*, 262–269. https://doi.org/10.1107/S002188989700811X

Wenk, H. R., Speziale, S., McNamara, A. K., & Garnero, E. J. (2006). Modeling lower mantle anisotropy development in a subducting slab. *Earth and Planetary Science Letters*, *245*(1–2), 302–314.

Wentzcovitch, R. M., Tsuchiya, T., & Tsuchiya, J. (2006). MgSiO3 postperovskite at *D*″ conditions. *Proceedings of the National Academy of Sciences of the United States of America*, *103*(3), 543–546. https://doi.org/10.1073/pnas.0506879103

Wookey, J., & Kendall, J. M. (2008). Constraints on lowermost mantle mineralogy and fabric beneath Siberia from seismic anisotropy. *Earth and Planetary Science Letters*, *275*, 32–42. https://doi.org/10.1016/j.epsl.2008.07.049

Wookey, J., Kendall, J.-M., & Rümpker, G. (2005). Lowermost mantle anisotropy beneath the North Pacific from differential S—ScS splitting. *Geophysical Journal International*, *161*, 829–838. https://doi.org/10.1111/j.1365-246X.2005.02623.x

Wookey, J., Stackhouse, S., Kendall, J.-M., Brodholt, J., & Price, G. D. (2005). Efficacy of the post-perovskite phase as an explanation for lowermost-mantle seismic properties. *Nature*, *438*(7070), 1004–1007. https://doi.org/10.1038/nature04345

Wu, X., Lin, J.-F., Kaercher, P., Mao, Z., Liu, J., Wenk, H.-R., & Prakapenka, V. B. (2017). Seismic anisotropy of the *D*″ layer induced by (001) deformation of post-perovskite. *Nature Communications*, *8*(1), 1–6. https://doi.org/10.1038/ncomms14669

Yamazaki, D., Yoshino, T., Ohfuji, H., Ando, J., & Yoneda, A. (2006). Origin of seismic anisotropy in the *D*″ layer inferred from shear deformation experiments on post-perovskite phase. *Earth and Planetary Science Letters*, *252*, 372–378. https://doi.org/10.1016/j.epsl.2006.10.004

Young, C. J., & Lay, T. (1990). Multiple phase analysis of the shear velocity structure in the *D*″ region beneath Alaska. *Journal of Geophysical Research*, *95*, 17,385–17,402. https://doi.org/10.1029/JB095iB11p17385

Young, C. J., & Lay, T. (1987). Evidence for a shear velocity discontinuity in the lower mantle beneath India and the Indian Ocean. *Physics of the earth and planetary interiors*, *49*(1-2), 37–53.